


RESEARCH ARTICLE | OCTOBER 16 2025

Low-temperature synthesis of Al-rich rock salt $\text{Cr}_{1-x}\text{Al}_x\text{N}$ films with selective metal ion bombardment by synchronized substrate bias pulsing

Sanath Kumar Honnali ; Robert Boyd ; Daniel Lundin ; Grzegorz Greczynski ; Ganpati Ramanath ; Per Eklund 



Appl. Phys. Lett. 127, 151906 (2025)

<https://doi.org/10.1063/5.0287938>



Articles You May Be Interested In

Metal versus rare-gas ion irradiation during $\text{Ti}_{1-x}\text{Al}_x\text{N}$ film growth by hybrid high power pulsed magnetron/dc magnetron co-sputtering using synchronized pulsed substrate bias

J. Vac. Sci. Technol. A (September 2012)

X-ray Photoelectron Spectroscopy Analyses of the Electronic Structure of Polycrystalline $\text{Ti}_{1-x}\text{Al}_x\text{N}$ Thin Films with $0 \leq x \leq 0.96$

Surf. Sci. Spectra (October 2014)

Extended metastable Al solubility in cubic VAIN by metal-ion bombardment during pulsed magnetron sputtering: film stress vs subplantation

J. Appl. Phys. (July 2017)

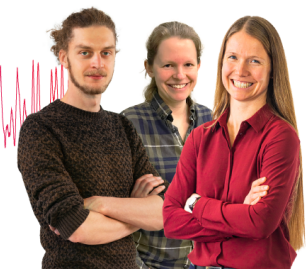
17 November 2025 09:23:23

Webinar From Noise to Knowledge

May 13th – Register now



Universität
Konstanz



Low-temperature synthesis of Al-rich rock salt $\text{Cr}_{1-x}\text{Al}_x\text{N}$ films with selective metal ion bombardment by synchronized substrate bias pulsing

Cite as: Appl. Phys. Lett. **127**, 151906 (2025); doi: 10.1063/5.0287938

Submitted: 27 June 2025 · Accepted: 1 October 2025 ·

Published Online: 16 October 2025



View Online



Export Citation



CrossMark

Sanath Kumar Honnali,^{1,2,a)} Robert Boyd,² Daniel Lundin,² Grzegorz Greczynski,²
Ganpati Ramanath,^{1,3,4} and Per Eklund^{1,2,4}

AFFILIATIONS

¹Inorganic Chemistry, Department of Chemistry—Ångström Laboratory, Uppsala University, SE-751 21 Uppsala, Sweden

²Thin Film Physics Division, Department of Physics, Chemistry and Biology (IFM), Linköping University, SE-581 83 Linköping, Sweden

³Materials Science and Engineering Department, Rensselaer Polytechnic Institute, Troy, New York 12180, USA

⁴Wallenberg Initiative in Materials Science for Sustainability, Department of Chemistry, Uppsala University, SE-751 21 Uppsala, Sweden

^{a)} Author to whom correspondence should be addressed: sanath-kumar.honnali@kemi.uu.se

ABSTRACT

We demonstrate a two-stage low-temperature ($<100^\circ\text{C}$) growth process for obtaining Al-rich rock salt-structured $\text{Cr}_{1-x}\text{Al}_x\text{N}$ films by high-power impulse magnetron sputtering (HiPIMS) with synchronized substrate bias pulsing. The first stage features selective $\sim 100\text{ eV}$ Al^+ ion irradiation that promotes out-of-plane (002) texture in rock salt $\text{Cr}_{0.3}\text{Al}_{0.7}\text{N}$. Film thickness was limited to $<\sim 230\text{ nm}$ above which wurtzite-AlN formation was observed. The second stage combines the synchronized bombardment of $\sim 100\text{ eV}$ Al^+ and Cr^+ ions, allowing the synthesis of rock salt $\text{Cr}_{1-x}\text{Al}_x\text{N}$ with unprecedentedly high Al contents up to $x \approx 0.7$ without wurtzite-AlN formation. Peening effects from heavier Cr^+ ions stabilize rock salt $\text{Cr}_{1-x}\text{Al}_x\text{N}$ with greater Al content, induce compressive stresses, and densify the film. In contrast, single-stage DC magnetron sputtering or HiPIMS using floating or continuous bias suffers from poor crystallinity, Ar entrapment, and film delamination. These findings establish that two-stage growth with selective ion bombardment is an attractive approach for tailoring stable single-phase Al-rich $\text{Cr}_{1-x}\text{Al}_x\text{N}$ coatings with controlled properties for applications that do not allow high temperature processing.

© 2025 Author(s). All article content, except where otherwise noted, is licensed under a Creative Commons Attribution (CC BY) license (<https://creativecommons.org/licenses/by/4.0/>). <https://doi.org/10.1063/5.0287938>

Single-phase rock salt-structured transition metal nitrides (TMNs) exhibit remarkable mechanical properties for applications as coatings on cutting tools and automotive components. Alloying Al into single-phase TMNs is known to enhance the thermal stability and mechanical properties.^{1–5} For instance, $\text{Cr}_{1-x}\text{Al}_x\text{N}$ ($x = \text{Al}/(\text{Al} + \text{Cr})$) offer increased thermal stability, resistance to wear^{6–9} and fatigue¹⁰ due to passivating Al_2O_3 and Cr_2O_3 formation.^{11,12} However, realizing dense micro-structured Al-rich rock salt TMN films by conventional physical vapor deposition requires high temperatures (e.g., $500 < T_{\text{dep}} \leq 800^\circ\text{C}$) at which the formation of thermodynamically more stable^{13,14} and softer wurtzite-aluminum nitride (w-AlN) limits Al solubility and degrades mechanical properties.

Low-temperature synthesis of TMNs precludes w-AlN formation but also limits the dissolved Al content. Rock salt-structured $\text{TM}_{1-x}\text{Al}_x\text{N}$ with $\text{TM} = \text{Ti}, \text{Zr}, \text{V},$ and Cr obtained by kinetically driven thin-film growth by DC magnetron sputtering (DCMS) at $T_{\text{dep}} \sim 500^\circ\text{C}$ feature dissolved Al in the $0.3 \leq x \leq 0.67$ range.^{15–18} Incorporating higher dissolved Al requires highly ionized fluxes obtainable in cathodic arc deposition^{1,19–21} and medium plasma density⁷ radio frequency magnetron sputtering.²²

Recent works have realized TMNs^{23–25} with high dissolved Al contents by high-power impulse magnetron sputtering (HiPIMS), which features high metal ion fluxes.^{26–30} $\text{Ti}_{1-x}\text{Al}_x\text{N}$ ^{31,32} and $\text{V}_{1-x}\text{Al}_x\text{N}$ deposited by HiPIMS at $T_{\text{dep}} = 500^\circ\text{C}$ show superior mechanical properties^{13,33,34}

and residual stress control compared to films obtained by DCMS.^{32,35,36} While low-temperature synthesis of rock salt $\text{Cr}_{1-x}\text{Al}_x\text{N}$ films with $x < \sim 0.6$ has been reported,^{12,37} realizing higher dissolved Al closer to the theoretical solubility limit $x \sim 0.75$ ^{38,39} without AlN formation is of interest for accessing superior properties.

In this Letter, we demonstrate low-temperature HiPIMS synthesis of rock salt $\text{Cr}_{1-x}\text{Al}_x\text{N}$ films with high dissolved Al in the $0.6 \leq x \leq 0.73$ range by a two-stage biasing film growth approach featuring selective and synchronized bombardment of ~ 100 eV Al^+ and Cr^+ ions. This strategy not only precludes w-AlN formation but also allows control over film stress and density. These attributes are not realized during continuous metal and gas ion irradiation in HiPIMS and Ar^+ bombardment during DCMS, which result in film delamination, low-crystallinity, and entrapped Ar. These findings are important for realizing Al-rich rock salt-structured single-phase $\text{Cr}_{1-x}\text{Al}_x\text{N}$ films with tunable stress and density on substrates requiring low-temperature processing.

$\text{Cr}_{1-x}\text{Al}_x\text{N}$ films were grown on 10×10 mm² pieces of Si(001) substrates by reactive magnetron sputtering in a $< \sim 4 \times 10^{-6}$ Pa base pressure ultra-high vacuum chamber. The substrates were ultrasonically cleaned successively in acetone and ethanol for 10 min each and blown dry with N_2 . Circular 3-in.-diameter alloy targets of Cr and Al (30:70) were sputtered in a 3 mTorr plasma created from a 99.9% pure 80/20 ratio Ar/N_2 mixture with 6 sccm N_2 and 23 sccm Ar. Prior to each deposition, the target was sputter-etched for 5 min with a 100 W HiPIMS discharge in Ar sustained at 2.5 mTorr.

$\text{Cr}_{1-x}\text{Al}_x\text{N}$ films were grown by unipolar HiPIMS in peak current control mode featuring $I_{\text{peak}} \sim 40$ A with a 25 μs pulse width at 100 W average power, with the HiPIMS pulses generated by a HiPSTER 1 (Ionautics AB) unit. Films were deposited either with a constant DC substrate bias $U_s^{\text{dc}} = -100$ V, floating potential ($V_{\text{float}} \approx -30$ V) or a pulsed substrate bias with amplitudes of $-100 \leq U_s^{\text{sync}} \leq -300$ V. Selective metal ion impingement was realized by synchronizing the substrate bias pulse to the target voltage U_{target} pulse with a 20 μs delay (t_{delay}). During film growth, the substrate was rotated at 5 rpm with no intentional heating, with a ~ 11 cm substrate-target distance, and a 30° substrate surface-magnetron surface normal angle. Reference DCMS films were grown at the same average power as HiPIMS with $U_s^{\text{dc}} = -100$ V.

X-ray diffractograms (XRD) were acquired using a PANalytical Empyrean diffractometer with Ni-filtered Cu K_α radiation ($\lambda = 0.15406$ nm) incident through a 6 mm divergent slit for $25^\circ \leq 2\theta \leq 90^\circ$ with a step size of 0.03° using a PIXcel^{3D}-Medipix3 detector. We also carried out θ - 2θ scans at sample tilts in the $20^\circ \leq \psi \leq 70^\circ$ range⁴⁰ with $\Delta\psi = 5^\circ$ steps in a Philips MRD diffractometer operated in point focus mode. Pole figures were acquired in the same diffractometer to study film texture by using a 2×2 mm² crossed slits in the incident-beam optics, and a parallel plate collimator in secondary optics.

Residual stresses were determined from Si(004) rocking curves measured at multiple locations on the Si using the Philips MRD diffractometer. A hybrid monochromator with a $1/32^\circ$ divergence slit was used to obtain a 0.09 mm probe beam exclusively comprised of $\text{Cu K}\alpha_1$ radiation. This, together with a parallel plate collimator with a 3-mm-wide receiving slit, provides a high angular resolution of $< 0.023^\circ$, eliminating thin-film corrections. Stress was extracted by inputting Si(001) biaxial modulus $M_{(100)} \sim 181$ GPa⁴¹ into a modified Stoney

equation.⁴² X-ray reflectivity (XRR) measurements in the same diffractometer were carried out to determine film density from the total external reflection critical angle using the X'Pert Reflectivity software. Film density was also verified by dividing the areal density obtained from Rutherford backscattering spectrometry (RBS) with the film thickness (t_{film}) measured by cross section scanning electron microscopy (SEM) images using ZEISS Sigma 300 operated at 3 kV.

Sample cross sections for scanning transmission electron microscopy (STEM) were prepared using a Gemini ZEISS 1540 XB dual beam SEM-focused ion beam (FIB) microscope system. A Pt protective layer was deposited on top of the films prior to FIB sectioning. Electron-transparent cross sections were analyzed by conventional TEM and STEM using an FEI Tecnai G2 TF 20 UT instrument operated at 200 kV. STEM images were collected using an 80–260 mrad range annular detector.

Film composition was measured by a combination of RBS and time-of-flight elastic recoil detection analysis (ToF-ERDA) measurements carried out using a Pelletron Tandem accelerator (5 MV NEC-5SDH-2).⁴³ The RBS spectra, obtained with 2 MeV primary He^+ ions incident at 5° to the film surface normal and backscattered atoms collected at 170° , were analyzed using SIMNRA⁴⁴ 7.03. ToF-ERDA measurements were conducted with 36 MeV $^{127}\text{I}^{8+}$ ions incident with a 67.5° angle to the film surface normal, and the recoils collected by a ToF-telescope and a gas ionization detector placed at 45° to the incident beam. Potku 2.2.4 code⁴⁵ was used to determine elemental composition depth profiles.

Selective metal ion acceleration requires synchronization of substrate bias pulses with the HiPIMS discharge pulse U_{target} by a time delay t_{delay} . We designed our bias pulses [Fig. 1(a)] based on the time-of-flight (ToF) recorded during similar HiPIMS discharges involving Cr, Al, and Cr:Al in the $10 \mu\text{s} \leq t \leq 110 \mu\text{s}$ regime captured by time-resolved mass spectrometry.^{46,47} The key feature is that lighter Al^+ ions arrive earlier (ToF $\approx 20 \mu\text{s}$) at the substrate than heavier Cr^+ and Ar^+ ions ($\sim 35 \mu\text{s}$). Thus, the ignition of the substrate bias pulse at $t = 20 \mu\text{s}$ [Fig. 1(b)] acts predominantly on the metal ions, and precludes excessive compressive stress induced by Ar^+ ions that typically dominate the ion flux during early stages.

Our analysis considers only singly charged metal ions, as amounts of doubly ionized species are expected to be low due to higher second ionization potentials of Cr and Al (16.54 and 18.89 eV, respectively)⁴⁸ than the first ionization potential of Ar (15.76 eV),⁴⁹ and the gas ions (N^+ and N_2^+) do not have a dominant effect on the phase stability due to their low mass. The temporal overlap between Cr^+ and Ar^+ ions precludes the exclusive use of Cr^+ ions to prevent residual stresses and film delamination caused by Ar during early stages of film growth.⁵⁰ We employ a two-stage biasing approach to minimize the deleterious effects of Ar^+ ions. The first stage features selective Al^+ ion bombardment followed by a second stage involving Al^+ , Cr^+ , and Ar^+ ions.

X-ray diffractograms from $\text{Cr}_{1-x}\text{Al}_x\text{N}$ films grown by HiPIMS with synchronized bias pulsing are presented in Fig. 2(a). Films grown with bias amplitude $U_s^{\text{sync-Al}^+} = -100$ V exhibit two Bragg peaks, corresponding to rock salt $\text{Cr}_{1-x}\text{Al}_x\text{N}(200)$ at $2\theta = 43.65^\circ$, and an asymmetric peak from w-AlN at $2\theta \approx 36^\circ$. Two-axis diffractometry and pole figure analyses (supplementary material Fig. S1) show that the asymmetric peak from w-AlN features a strong AlN(002) reflection at $2\theta = 35.5^\circ$ and a weak AlN(101) peak at $2\theta \approx 37^\circ$. Higher bias

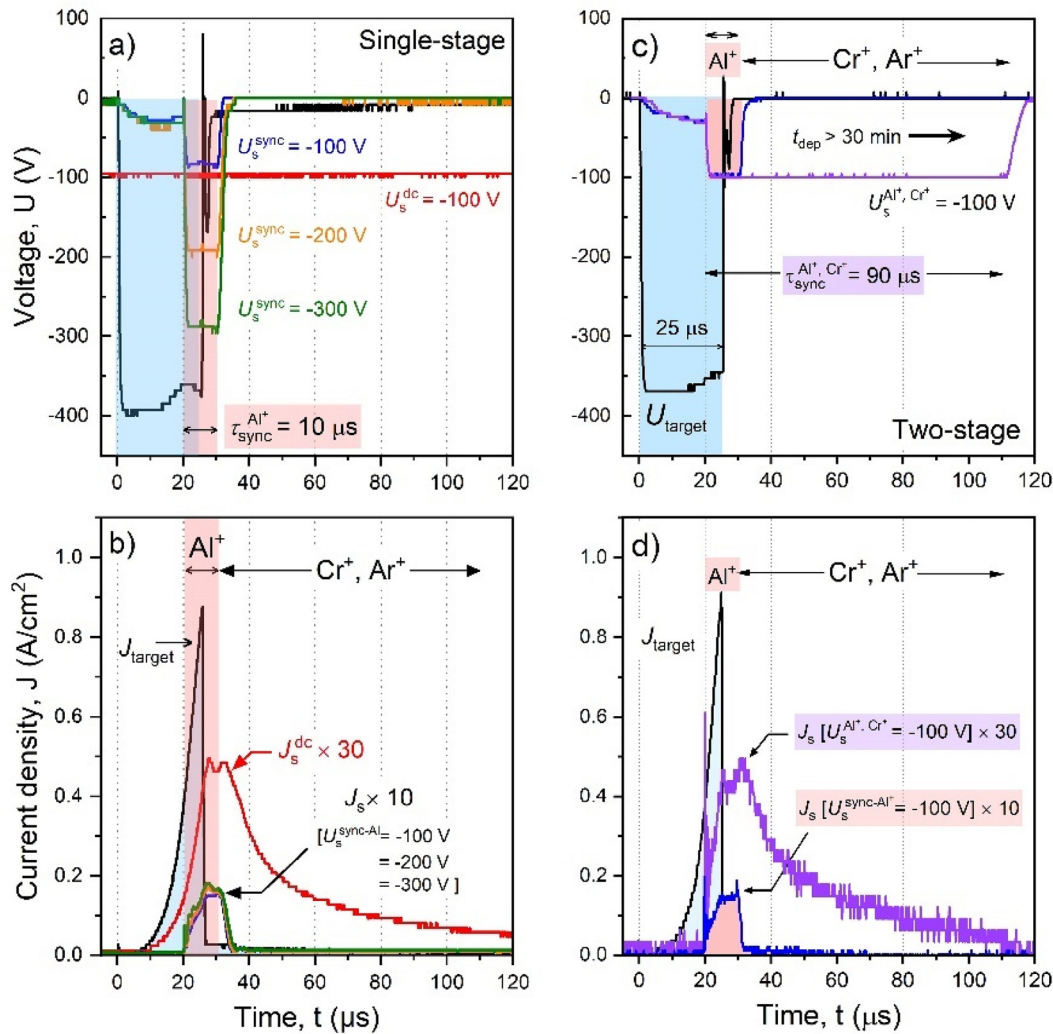


FIG. 1. Waveforms of (a) target and substrate voltage and (b) current density showing HiPIMS (blue shaded) and synchronized substrate bias (red shaded) pulses that accelerate Al^+ ions in a single-stage process. The substrate bias current density J_s^{dc} and J_s are enhanced thirtyfold and tenfold, respectively, for clarity. (c) Substrate bias and (d) current density waveforms that accelerate Al^+ and combined Al^+ , Cr^+ ions to the same amplitude in a two-stage process. The subscript "s" denotes the substrate.

amplitudes of $-200 \text{ V} \leq U_s^{\text{sync-Al}^+} \leq -300 \text{ V}$ produce single-phase rock salt $\text{Cr}_{1-x}\text{Al}_x\text{N}$ films with no evidence of w-AlN. However, these films showed significant cracking and delamination. Moreover, the broad low intensity peaks indicate lower crystallinity, likely due to greater ion-induced damage at larger bias amplitudes. Films deposited by conventional DCMS with $U_s^{\text{dc}} = -100 \text{ V}$ also exhibit very broad peaks, indicating poor crystallinity [Fig. 2(a)]. These are in stark contrast to highly textured films obtained by HiPIMS with $U_s^{\text{dc}} = -100 \text{ V}$ indicated by an intense and narrow (111) Bragg reflection corresponding to rock salt $\text{Cr}_{1-x}\text{Al}_x\text{N}$ phase (powder diffraction file #020-0801).

Compositions of $\text{Cr}_{1-x}\text{Al}_x\text{N}$ films synthesized by HiPIMS determined from RBS and ToF-ERDA for $-100 \text{ V} \leq U_s^{\text{sync-Al}^+} \leq -300 \text{ V}$ are summarized in Fig. 2(b). The nominal film composition was $\text{Cr}_{0.3}\text{Al}_{0.7}\text{N}$ (i.e., $x = 0.7$) with $\sim 1 \pm 0.2$ at. % oxygen and argon and ~ 0.2 at. % carbon with no observable dependence

on $U_s^{\text{sync-Al}^+}$. Films deposited by DCMS with $U_s^{\text{dc}} = -100 \text{ V}$ were slightly understoichiometric with $\text{N}/(\text{Al}+\text{Cr}) = 0.95$ and about 10.4% higher in Cr than nominal ($1-x = 0.3$). Films deposited by HiPIMS with $U_s^{\text{dc}} = -100 \text{ V}$ showed severe understoichiometry with $\text{N}/(\text{Al}+\text{Cr}) = 0.66$ but are Al-rich as indicated by $\text{Cr}_{0.1}\text{Al}_{0.5}\text{N}_{0.4}$, i.e., $x = 0.83$.

The observed compositional differences can be traced to ion-induced effects. HiPIMS with synchronized bias pulsing with $U_s^{\text{sync-Al}^+} = -100 \text{ V}$ entails a high flux Al^+ ions bombardment. Increasing the Al^+ ion energy by adjusting $U_s^{\text{sync-Al}^+}$ alters film growth kinetics as seen from decreases in the film thickness from 590 to 520 nm. However, the dissolved Al content x is unchanged, suggesting that the momentum transfer from light Al^+ ions is insufficient to alter film composition. In contrast, HiPIMS with U_s^{dc} yields Al-rich and N-deficient films likely due to nonselective bombardment of Al^+ , Cr^+ , and Ar^+ ions causing

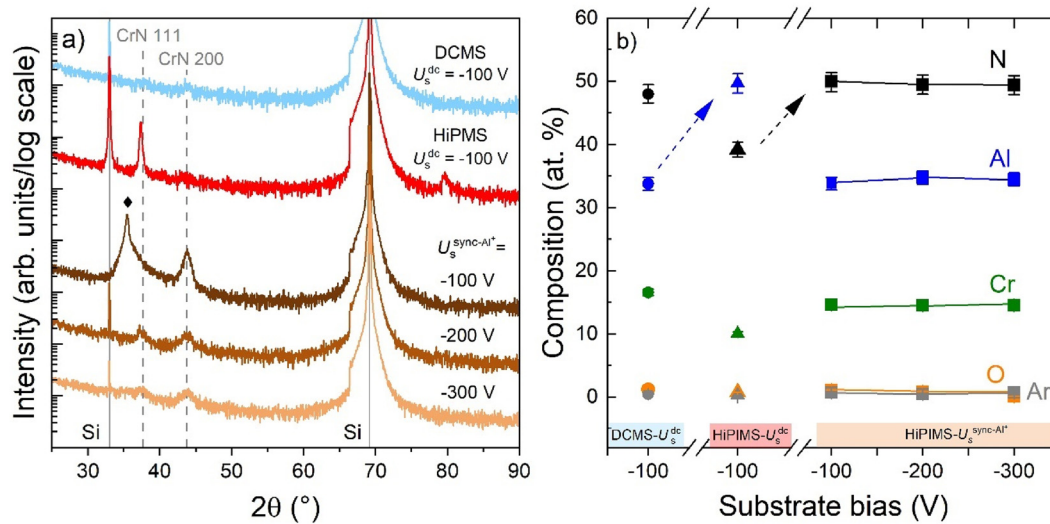


FIG. 2. (a) X-ray diffractograms obtained by symmetric θ - 2θ scans from $\text{Cr}_{1-x}\text{Al}_x\text{N}$ films grown by DCMS and HiPMS with a DC bias of -100 V and HiPMS with synchronized Al^+ irradiation. The \blacklozenge symbol indicates Bragg peak from $w\text{-AlN}(002)$. (b) Elemental compositions of $\text{Cr}_{1-x}\text{Al}_x\text{N}$ films from RBS and ToF-ERDA analyses. Al and Cr compositional uncertainties are smaller than the symbol dimensions.

preferential sputter etching of Cr and N from the film surface (see sputter yields listed in [supplementary material Table S1](#) from TRIM⁵¹). This view is supported by efficient momentum transfer from Ar^+ and Cr^+ ions to Cr than to Al (see [supplementary material Fig. S3](#)). DCMS involves \sim a few %^{29,52} metal ions, wherein sputter etching by Ar^+ ions dominates and slightly depletes the Al content [Fig. 2(b)].

Scanning transmission electron microscopy (STEM) images from $\text{Cr}_{1-x}\text{Al}_x\text{N}$ films grown by HiPMS with $U_s^{\text{sync-Al}^+} = -100$ V reveal a featureless homogeneous bottom layer that transitions into a heterogeneous top layer [Fig. 3(a)]. The top layer consists of alternating nano-scale regions of bright and dark contrast with different atomic arrangements separated by vertically oriented pores [Fig. 3(b)].

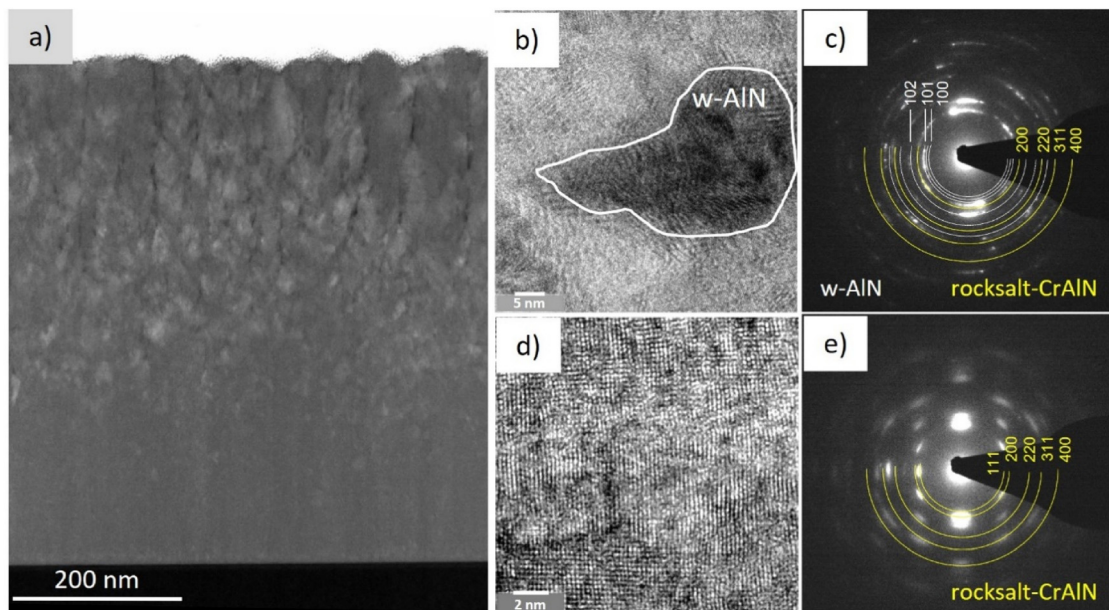


FIG. 3. (a) Cross section STEM images from a $\text{Cr}_{1-x}\text{Al}_x\text{N}$ film grown by HiPMS with $U_s^{\text{sync-Al}^+} = -100$ V. (b) HRTEM image and (c) electron diffraction pattern from the top layer. The highlighted region corresponds to $w\text{-AlN}$. (d) HRTEM image and (e) electron diffraction pattern from the bottom layer. Yellow miller indices connote rock salt CrAlN and white indices refer to $w\text{-AlN}$.

In contrast, the bottom layer shows uniform atomic stacking as expected in rock salt $\text{Cr}_{1-x}\text{Al}_x\text{N}$ [Fig. 3(d)].

Electron diffraction patterns from the top layer reveal Bragg reflections from rock salt $\text{Cr}_{1-x}\text{Al}_x\text{N}$ and w-AlN [Fig. 3(c)]. The bottom layer shows only rock salt $\text{Cr}_{1-x}\text{Al}_x\text{N}$ with a strong out-of-plane (200) texture [Fig. 3(e)], consistent with the XRD results. RBS measurements showing up to ~ 2.3 at. % Ar in the bottom homogeneous layer suggests that the (200) texture facilitates Ar^+ channeling.⁵³ The $< \sim 0.7$ at. % Ar in the top layer indicates that the heterogeneous microstructure diminishes Ar^+ channeling. ToF-ERDA analyses [Fig. 2(b)] indicating a higher oxygen (~ 1.1 at. %) in the top layer than in the bottom layer (the $< \sim 0.5$ at. %) is likely due to microporosity in the top layer. In contrast, HiPIMS film with DC bias shows a 10-nm-thick Ar rich layer near the film/substrate interface that correlates with the tendency of the films to delaminate (see [supplementary material Fig. S2](#)).

The biasing modality (synchronized pulsing vs constant DC) and the synthesis mode (DCMS vs HiPIMS) impact film density. Film density was obtained by dividing the areal density extracted from RBS with the film thickness measured by SEM and compared with the density obtained from the total external reflection critical angle in XRR. Films deposited by DCMS and HiPIMS with synchronized pulsing show similar densities in the $3.1\text{--}3.7\text{ g/cm}^3$ range [Fig. 4(a)]. This density range is 7%–23% lower than the $\sim 4\text{ g/cm}^3$ theoretical density of rock salt $\text{Cr}_{0.3}\text{Al}_{0.7}\text{N}$, consistent with microporosity indicated by STEM measurements. Underdense films with $x < \sim 0.7$ obtained by DCMS and HiPIMS with synchronized bias pulsing are not entirely unexpected due to low mass ion irradiation.⁵⁴

The high Al content ($x = 0.83$) and N-deficiency in the film synthesized by HiPIMS with DC bias indicated by ToF-ERDA [Fig. 2(b)] foster closer metal cation packing. While lattice expansion in the growth direction due to in-plane compressive strain would slightly reduce the XRR-derived density, this effect is restricted to the beam spot size, which is small compared to the wafer bending scale. The

main factors for the high XRR-derived density of 4.5 g/cm^3 are the volume shrinkage from Al-rich, N-deficient composition together with surface Cr-enrichment as indicated by RBS [see [supplementary material Fig. S2\(b\)](#)], both of which increase the local electron density and, consequently, the film density.

The influences of different biasing strategies on film thickness and residual stress are illustrated in Fig. 4(b). The decrease in $\text{Cr}_{1-x}\text{Al}_x\text{N}$ film thickness upon increasing $U_s^{\text{sync-Al}^+}$ from -100 to -300 V correlates with densification and re-sputtering effects described above. The films grown by HiPIMS U_s^{sync} exhibit lower residual stresses between ~ -0.14 and -0.6 GPa than -0.7 GPa seen in films grown by DCMS. However, HiPIMS films grown with a -100 V DC bias delaminated, leaving behind an $\sim 200\text{-nm}$ -thick film with a residual stress of -2.1 GPa (see [supplementary material Fig. S2](#)). Such delamination is a consequence of stress buildup from continuous Cr^+ and Ar^+ ion bombardment, which generates point defects that induce excessive strain.⁵⁵ In comparison, Al^+ bombardment primarily transfers momentum to Al atoms with minimal impact on Cr (see [supplementary material Fig. S3](#)) and helps maintain lower stress levels but at the cost of film quality, as it leads to a porous microstructure [Fig. 3(a)].

To ensure single-phase cubic $\text{Cr}_{1-x}\text{Al}_x\text{N}$, we set the deposition duration to be 30 min in the first stage of our process using Al^+ ion bombardment, based on STEM analysis showing w-AlN formation at higher deposition times [Fig. 3(a)]. The second stage involves synchronized Al^+ , Cr^+ , and Ar^+ ion bombardment on top of an $\sim 230\text{-nm}$ -thick $\text{Cr}_{1-x}\text{Al}_x\text{N}$ layer [Fig. 5(a)]. This was achieved by extending the bias pulse width from 10 to $90\ \mu\text{s}$ during continuous film growth. X-ray diffractograms [Fig. 5(b)] from the stage-one layer with and without a 70-nm -thick stage-two layer exhibit out-of-plane (200) texture. Continuing stage-two growth for another 55 min (total $t_{\text{dep}} = 100\text{ min}$) results in $\sim 470\text{-nm}$ -thick polycrystalline $\text{Cr}_{1-x}\text{Al}_x\text{N}$ films with a (111) texture.

The (200) to (111) texture change is related to the linear increase in compressive stress with film thickness [Fig. 5(c)]. For thicknesses

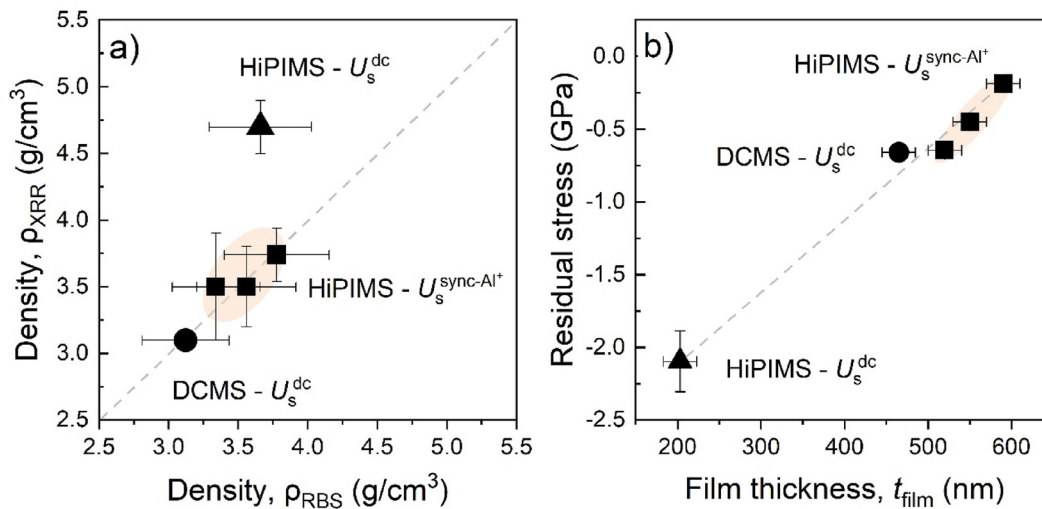


FIG. 4. (a) Film density measured from XRR plotted vs density deduced from RBS and SEM. (b) Residual stress as a function of film thickness. The dotted line is a linear fit to the data points.

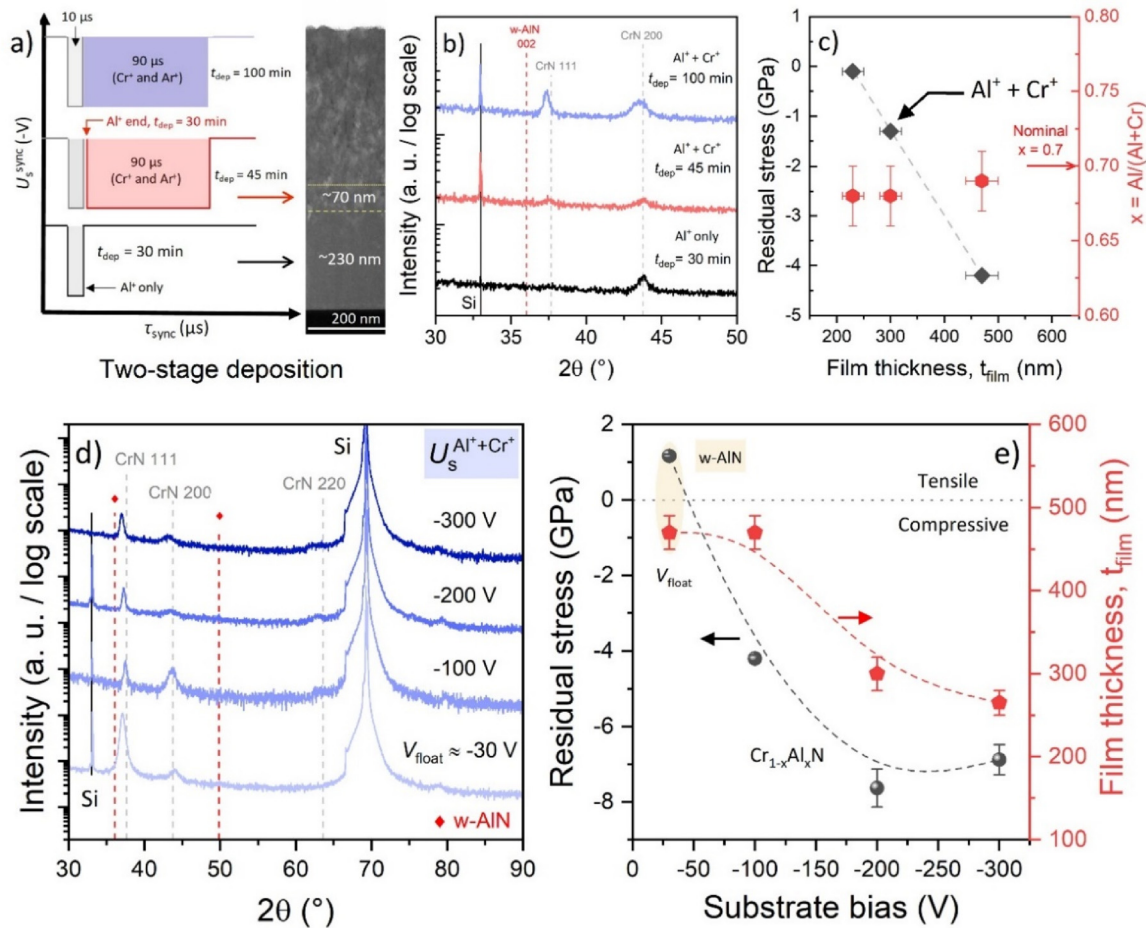


FIG. 5. (a) Schematic depiction of the two-stage deposition strategy for growing rock salt $\text{Cr}_{1-x}\text{Al}_x\text{N}$ films without w-AlN using Al^+ ion bombardment in the first stage, and Cr^+ and Al^+ ion bombardment in the second stage. (b) X-ray diffractograms (θ - 2θ scans) from films obtained by this strategy at three different deposition times. (c) Film stress evolution and Al metal fraction x plotted as a function of film thickness. (d) X-ray diffractograms from films grown with the two-stage HiPIMS approach with synchronized bias amplitudes in the $-100 \text{ V} \leq U_s^{\text{Al}^+, \text{Cr}^+} \leq -300 \text{ V}$ range compared to film grown by HiPIMS with a floating bias of -30 V . (e) Residual stress and film thickness in films grown by the two-approach as a function of substrate bias. The lines are only a guide to the eye.

$< \sim 300 \text{ nm}$, the compressive stress increases are attributable to sub-plantation effects in the first few nanometers below the surface (see qualitative TRIM simulations Fig. S3) and defect generation from energetic Cr^+ ions deeper along the open (200) channels. These mechanisms cannot explain increased stress accumulation for film thicknesses above 300 nm. While continued atomic peening from ~ 100 to 300 eV Cr^+ and Al^+ ions delivers significant momentum to increase intrinsic compressive stresses, thermal stress relaxation is minimal due to low temperatures ($T_s < 100^\circ\text{C}$), consistent in rock salt TMNs.^{53,56-60} The accumulated stress raises the strain energy sufficiently to induce grain reorientation, which promotes densification of the columnar microstructure (see supplementary material Fig. S5) and the formation of new grain boundaries, thereby minimizing surface energy and favoring the development of a preferred out-of-plane (111) orientation while maintaining the metal ratios at $x = 0.68 \pm 0.01$.

X-ray diffractograms from $\text{Cr}_{1-x}\text{Al}_x\text{N}$ ($0.62 \leq x \leq 0.73$) films grown by HiPIMS using a two-stage growth strategy at different

synchronized bias amplitudes $-100 \text{ V} \leq U_s^{\text{Al}^+, \text{Cr}^+} \leq -300 \text{ V}$ [Fig. 5(d)] indicate a rock salt $\text{Cr}_{1-x}\text{Al}_x\text{N}$ phase with randomly oriented crystallites. Increasing the $U_s^{\text{Al}^+, \text{Cr}^+}$ shifts the (111) peak to lower angles due to compositional differences and residual stress generation. A reference film grown at V_{float} where all ionized species have an energy $E_{\text{ions}} \approx 30 \text{ eV}$, shows four Bragg peaks attributed to two different phases. Two-axis XRD measurements confirm the presence of wurtzite-AlN as the major phase and rock salt $\text{Cr}_{1-x}\text{Al}_x\text{N}$ as the minor phase (see supplementary material Fig. S4).

As the $U_s^{\text{Al}^+, \text{Cr}^+}$ amplitude increases [Fig. 5(e)], compressive stress builds up in the rock salt $\text{Cr}_{1-x}\text{Al}_x\text{N}$ films up to $-4.2 \pm 0.1 \text{ GPa}$ for the same film thickness undergoing densification ($\rho_{\text{XRR}} = 4.6 \pm 0.1$ and $\rho_{\text{RBS}} = 4.5 \pm 0.2 \text{ g/cm}^3$) with no film delamination and no Cr-surface enrichment. However, the as-deposited film at $U_s^{\text{Al}^+, \text{Cr}^+} = -200 \text{ V}$ with $-7.6 \pm 0.5 \text{ GPa}$ stress delaminates with $x = 0.66$ and $N/(\text{Al}+\text{Cr}) = 1.08$. The film obtained with $U_s^{\text{Al}^+, \text{Cr}^+} = -300 \text{ V}$ exhibits $x = 0.73$ and $N/(\text{Al}+\text{Cr}) = 0.72$ and a stress of $-6.8 \pm 0.4 \text{ GPa}$.

Adhesion tape tests on this reveal no observable peeling, indicating good adhesion. These results highlight the influence of ion energies on film composition, stress, and adhesion.

In contrast, HiPIMS films grown at V_{float} show tensile stress due to w-AlN formation by low energy ion bombardment (~ 30 eV). We note that the dynamics of defect generation/annihilation by ~ 30 – 300 eV Cr^+ ions at low growth temperatures (e.g., $T_s < 100^\circ\text{C}$) is likely to be vastly different from that reported for film growth involving high temperatures and/or with high-energy/heavy ion fluxes.^{61–63} Thus, our results show that two-stage biasing enables independent control of bias pulse width, delay, and metal ion energies to stabilize rock salt $\text{Cr}_{1-x}\text{Al}_x\text{N}$ and is adaptable to other ternary transition metal nitrides (TM = Ti, Zr, V) based on the ToF of the ions to tailor composition, stress, and density.

To summarize, we demonstrated the low-temperature ($< 100^\circ\text{C}$) growth of single-phase Al-rich rock salt $\text{Cr}_{1-x}\text{Al}_x\text{N}$ films with $0.62 \leq x \leq 0.73$ using a two-stage HiPIMS-based synchronized substrate bias pulsing strategy involving high-energy Al^+ and Cr^+ ion bombardment. The first stage of film growth features selective Al^+ ion bombardment to obtain rock salt $\text{Cr}_{1-x}\text{Al}_x\text{N}$ formation without Ar trapping and delamination, and the film thickness is limited to < 230 nm to preclude wurtzite-AlN formation. The second stage involves increasing the Cr^+ ion energy without halting the film growth, which stabilizes rock salt $\text{Cr}_{1-x}\text{Al}_x\text{N}$ with high Al contents up to $x \sim 0.7$ and fosters compressive stress without delamination or large compositional changes. These features were not achievable with floating- or DC-biased films in HiPIMS or DCMS. Our two-stage biasing strategy utilizing synchronized substrate bias pulsing is attractive for realizing Al-rich rock salt $\text{Cr}_{1-x}\text{Al}_x\text{N}$ films with control over stress, composition, microstructure, and hence mechanical properties.

See the [supplementary material](#) includes sputter yields (Table S1), two-axis XRD scans and pole figures (Fig. S1), film delamination and microstructures of HiPIMS film with DC bias (Fig. S2), TRIM recoil simulations (Fig. S3) highlighting effects of Al^+ , Cr^+ , and Ar^+ projectiles, two-axis XRD scans confirming w-AlN phase formation in reference film under two-stage biasing growth strategy (Fig. S4) and cross section scanning electron microscope images (Fig. S5).

The work was financially supported by the VINNOVA Competence Centre FunMat-II Grant No. 2022-03071, the Swedish Government Strategic Research Area in Materials Science on Functional Materials at Linköping University (Faculty Grant SFO-Mat-LiU No. 2009 00971), the Knut and Alice Wallenberg Foundation through the Wallenberg Academy Fellows program (KAW-2020.0196), the Swedish Research Council (VR project 2021-03826), and the Swedish Energy Agency (Project 52740-1). This work was partially supported by the Wallenberg Initiative Materials Science for Sustainability (WISE) funded by the Knut and Alice Wallenberg Foundation, Swedish Research Council VR project 2024-04996, the U.S. National Science Foundation grant CMMI 2135725 through the BRITE program, and the Empire State Development's Division of Science, Technology and Innovation Focus Center at RPI, C210117. We gratefully acknowledge Daniel Primetzhofer and Robert Frost for RBS and ToF-ERDA measurements at Tandem laboratory supported by the Swedish Research Council (VR-RFI 2019_00191). SKH acknowledges

Rommel Paulo Viloan, Linköping University for assistance with the deposition chamber.

AUTHOR DECLARATIONS

Conflict of Interest

The authors have no conflicts to disclose.

Author Contributions

Sanath Kumar Honnali: Conceptualization (lead); Data curation (lead); Formal analysis (lead); Investigation (lead); Software (lead); Writing – original draft (lead). **Robert Boyd:** Formal analysis (equal); Investigation (equal). **Daniel Lundin:** Conceptualization (equal); Funding acquisition (equal); Resources (equal); Supervision (equal); Writing – review & editing (supporting). **Grzegorz Greczynski:** Formal analysis (equal); Funding acquisition (equal); Supervision (equal); Writing – review & editing (supporting). **Ganpati Ramanath:** Validation (equal); Writing – review & editing (equal). **Per Eklund:** Funding acquisition (lead); Project administration (lead); Resources (equal); Supervision (lead); Writing – review & editing (equal).

DATA AVAILABILITY

The data that support the findings of this study are available from the corresponding author upon reasonable request.

REFERENCES

- ¹A. Hörling, L. Hultman, M. Odén, J. Sjöln, and L. Karlsson, *J. Vac. Sci. Technol. A* **20**(5), 1815–1823 (2002).
- ²O. Knotek, M. Böhmer, and T. Leyendecker, *J. Vac. Sci. Technol. A* **4**(6), 2695–2700 (1986).
- ³P. H. Mayrhofer, A. Hörling, L. Karlsson, J. Sjöln, T. Larsson, C. Mitterer, and L. Hultman, *Appl. Phys. Lett.* **83**(10), 2049–2051 (2003).
- ⁴L. Hultman, *Vacuum* **57**, 1–30 (2000).
- ⁵R. Lamni, R. Sanjinés, M. Parlinska-Wojtan, A. Karimi, and F. Lévy, *J. Vac. Sci. Technol. A* **23**(4), 593–598 (2005).
- ⁶E. Spain, J. C. Avelar-Batista, M. Letch, J. Housden, and B. Lerga, *Surf. Coat. Technol.* **200**(5), 1507–1513 (2005).
- ⁷L. Wang, G. Zhang, R. J. K. Wood, S. C. Wang, and Q. Xue, *Surf. Coat. Technol.* **204**(21), 3517–3524 (2010).
- ⁸Y.-S. Yang, T.-P. Cho, and J.-H. Lin, *Thin Solid Films* **544**, 612–616 (2013).
- ⁹M. Uchida, N. Nihira, A. Mitsuo, K. Toyoda, K. Kubota, and T. Aizawa, *Surf. Coat. Technol.* **177–178**, 627–630 (2004).
- ¹⁰C. Brecher, G. Spachtholz, K. Bobzin, E. Lugscheider, O. Knotek, and M. Maes, *Surf. Coat. Technol.* **200**, 1738–1744 (2005).
- ¹¹K. Bobzin, N. Bagcivan, P. Immich, S. Bolz, R. Cremer, and T. Leyendecker, *Thin Solid Films* **517**, 1251–1256 (2008).
- ¹²J. Lin, B. Mishra, J. J. Moore, and W. D. Sproul, *Surf. Coat. Technol.* **202**(14), 3272–3283 (2008).
- ¹³G. Greczynski, S. Mráz, M. Hans, D. Primetzhofer, J. Lu, L. Hultman, and J. M. Schneider, *J. Appl. Phys.* **121**(17), 171907 (2017).
- ¹⁴L. Chen, Y. Du, P. H. Mayrhofer, S. Q. Wang, and J. Li, *Surf. Coat. Technol.* **202**(21), 5158–5161 (2008).
- ¹⁵U. Wahlström, L. Hultman, J. E. Sundgren, F. Adibi, I. Petrov, and J. E. Greene, *Thin Solid Films* **235**(1), 62–70 (1993).
- ¹⁶Y. Makino, M. Mori, S. Miyake, K. Saito, and K. Asami, *Surf. Coat. Technol.* **193**(1), 219–222 (2005).
- ¹⁷F. Rovere, D. Music, S. Ershov, M. t. Baben, H.-G. Fuss, P. H. Mayrhofer, and J. M. Schneider, *J. Phys. D* **43**(3), 035302 (2010).
- ¹⁸A. Sugishima, H. Kajioka, and Y. Makino, *Surf. Coat. Technol.* **97**(1), 590–594 (1997).

- ¹⁹H. Hasegawa, M. Kawate, and T. Suzuki, *Surf. Coat. Technol.* **200**(7), 2409–2413 (2005).
- ²⁰J. M. Andersson, J. Vetter, J. Müller, and J. Sjöln, *Surf. Coat. Technol.* **240**, 211–220 (2014).
- ²¹M. Kawate, A. Kimura, and T. Suzuki, *J. Vac. Sci. Technol. A* **20**(2), 569–571 (2002).
- ²²Y. Makino and K. Nogi, *Surf. Coat. Technol.* **98**(1), 1008–1012 (1998).
- ²³G. Greczynski, J. Lu, M. P. Johansson, J. Jensen, I. Petrov, J. E. Greene, and L. Hultman, *Surf. Coat. Technol.* **206**, 4202–4211 (2012).
- ²⁴G. Greczynski, S. Mráz, H. Ruess, M. Hans, J. Lu, L. Hultman, and J. M. Schneider, *J. Appl. Phys.* **122**(2), 25304 (2017).
- ²⁵G. Greczynski, J. Lu, J. Jensen, I. Petrov, J. E. Greene, S. Bolz, W. Kölker, C. Schiffrs, O. Lemmer, and L. Hultman, *Thin Solid Films* **556**, 87–98 (2014).
- ²⁶J. Bohlmark, M. Lattemann, J. T. Gudmundsson, A. P. Ehasarian, Y. Aranda Gonzalvo, N. Brenning, and U. Helmersson, *Thin Solid Films* **515**, 1522–1526 (2006).
- ²⁷D. Lundin, M. Čada, and Z. Hubička, *Plasma Sources Sci. Technol.* **24**(3), 035018 (2015).
- ²⁸M. Čada, N. Britun, A. Hecimovic, J. T. Gudmundsson, and D. Lundin, in *High Power Impulse Magnetron Sputtering*, edited by D. Lundin, T. Minea, and J. T. Gudmundsson (Elsevier, 2020), pp. 111–158.
- ²⁹T. Kubart, M. Čada, D. Lundin, and Z. Hubička, *Surf. Coat. Technol.* **238**, 152–157 (2014).
- ³⁰U. Helmersson, M. Lattemann, J. Bohlmark, A. P. Ehasarian, and J. T. Gudmundsson, *Thin Solid Films* **513**(1), 1–24 (2006).
- ³¹G. Greczynski, I. Petrov, J. E. Greene, and L. Hultman, *J. Vac. Sci. Technol. A* **37**, 60801 (2019).
- ³²G. Greczynski, J. Lu, J. Jensen, I. Petrov, J. E. Greene, S. Bolz, W. Kölker, C. Schiffrs, O. Lemmer, and L. Hultman, *J. Vac. Sci. Technol. A* **30**(6), 061504 (2012).
- ³³G. Greczynski, S. Mráz, L. Hultman, and J. M. Schneider, *Sci. Rep.* **7**(1), 17544 (2017).
- ³⁴G. Greczynski, S. Mráz, J. M. Schneider, and L. Hultman, *J. Appl. Phys.* **127**(18), 180901 (2020).
- ³⁵I. Petrov, L. Hultman, J. E. Sundgren, and J. E. Greene, *J. Vac. Sci. Technol.* **10**, 265–272 (1992).
- ³⁶G. Håkansson, J.-E. Sundgren, D. McIntyre, J. E. Greene, and W.-D. Münz, *Thin Solid Films* **153**, 55–65 (1987).
- ³⁷S. Hofmann and H. A. Jehn, *Mater. Corros.* **41**(12), 756–760 (1990).
- ³⁸Y. Makino, *ISIJ Int.* **38**(9), 925–934 (1998).
- ³⁹P. H. Mayrhofer, D. Music, T. Reeswinkel, H. G. Fuß, and J. M. Schneider, *Acta Mater.* **56**(11), 2469–2475 (2008).
- ⁴⁰M. Birkholz and C. Genzel, in *Thin Film Analysis by X-Ray Scattering* (Wiley, 2005), pp. 239–295.
- ⁴¹G. C. A. M. Janssen, M. M. Abdalla, F. van Keulen, B. R. Pujada, and B. van Venrooy, *Thin Solid Films* **517**, 1858–1867 (2009).
- ⁴²G. G. Stoney and C. A. Parsons, *Proc. R. Soc. London, Ser. A* **82**(553), 172–175 (1909).
- ⁴³P. Ström and D. Primetzhofer, *JINST* **17**, P04011 (2022).
- ⁴⁴M. Mayer, “SIMNRA user’s guide,” Report No. IPP 9/113 (Max-Planck-Institut für Plasmaphysik, Garching, Germany, 1997).
- ⁴⁵K. Arstila, J. Julin, M. I. Laitinen, J. Aalto, T. Konu, S. Kärkkäinen, S. Rahkonen, M. Raunio, J. Itkonen, J.-P. Santanen, T. Tuovinen, and T. Sajavaara, *Nucl. Instrum. Methods Phys. Res., Sect. B* **331**, 34–41 (2014).
- ⁴⁶G. Greczynski, I. Zhirkov, I. Petrov, J. E. Greene, and J. Rosen, *J. Vac. Sci. Technol. A* **36**(2), 020602 (2018).
- ⁴⁷H. Du, M. Zanaška, U. Helmersson, and D. Lundin, *Surf. Coat. Technol.* **454**, 129153 (2023).
- ⁴⁸K. Huo, D. Lundin, J. T. Gudmundsson, M. A. Raadu, J. W. Bradley, and N. Brenning, *J. Phys. D* **50**(35), 354003 (2017).
- ⁴⁹G. Greczynski, I. Petrov, J. E. Greene, and L. Hultman, *Vacuum* **116**, 36–41 (2015).
- ⁵⁰F. Cemin, G. Abadias, T. Minea, and D. Lundin, *Thin Solid Films* **688**, 137335 (2019).
- ⁵¹J. F. Ziegler, M. D. Ziegler, and J. P. Biersack, *Nucl. Instrum. Methods Phys. Res., Sect. B* **268**, 1818–1823 (2010).
- ⁵²I. Petrov, A. Myers, J. E. Greene, and J. R. Abelson, *J. Vac. Sci. Technol. A* **12**, 2846–2854 (1994).
- ⁵³I. Petrov, P. B. Barna, L. Hultman, and J. E. Greene, *J. Vac. Sci. Technol. A* **21**, S117–S128 (2003).
- ⁵⁴G. Greczynski, J. Lu, S. Bolz, W. Kölker, C. Schiffrs, O. Lemmer, I. Petrov, J. E. Greene, and L. Hultman, *J. Vac. Sci. Technol.* **32**, 41515 (2014).
- ⁵⁵A. V. Pshyk, I. Petrov, B. Bakhit, J. Lu, L. Hultman, and G. Greczynski, *Mater. Des.* **227**, 111753 (2023).
- ⁵⁶D. Holec, F. Rovere, P. H. Mayrhofer, and P. B. Barna, *Scr. Mater.* **62**(6), 349–352 (2010).
- ⁵⁷D. Dobrev, *Thin Solid Films* **92**(1), 41–53 (1982).
- ⁵⁸Y. Lv, L. Ji, X. Liu, H. Li, H. Zhou, and J. Chen, *Appl. Surf. Sci.* **258**(8), 3864–3870 (2012).
- ⁵⁹G. Abadias, *Surf. Coat. Technol.* **202**(11), 2223–2235 (2008).
- ⁶⁰G. Abadias, W. P. Leroy, S. Mahieu, and D. Depla, *J. Phys. D* **46**(5), 055301 (2013).
- ⁶¹J. H. Markna, R. N. Parmar, D. G. Kuberkar, R. Kumar, D. S. Rana, and S. K. Malik, *Appl. Phys. Lett.* **88**(15), 152503 (2006).
- ⁶²J. H. Markna, R. N. Parmar, D. S. Rana, K. Ravi, P. Misra, L. M. Kukreja, D. G. Kuberkar, and S. K. Malik, *Nucl. Instrum. Methods Phys. Res., Sect. B* **256**(2), 693–697 (2007).
- ⁶³R. N. Parmar, J. H. Markna, D. G. Kuberkar, R. Kumar, D. S. Rana, V. C. Bagve, and S. K. Malik, *Appl. Phys. Lett.* **89**(20), 202506 (2006).